Inverse Models and Harmonics Compensation for Suppressing Torque Ripples of Multiphase Permanent Magnet Motor

Lei Li, Kok-Meng Lee, *Fellow, IEEE*, Kun Bai, *Member, IEEE*, Xiaoping Ouyang, and Huayong Yang

***Abstract*—This paper presents two methods to derive an inverse model in harmonic forms for analyzing the interactions between the torque/current gains and currents, and for suppressing the torque ripples of a multiphase permanent magnet (PM) motor. The first method directly calculates the desired current harmonics from a pseudo-inverse model of a multiphase PM motor with no input-voltage saturation, which is independent of its rotor displacements, for torque ripple compensation. The second is an iterative-free method formulating the inverse model as an optimization problem that minimizes the copper loss subject to torque constraints while accounting for the effects of the input-voltage saturation. The formulation and significance of the two methods are illustrated with a multiphase PM motor for which published measurements are available for model validation and compared with three other commonly used current waveforms for benchmark comparison in terms of torque-ripples and copper losses.**

***Index Terms*—Harmonics, inverse model, PM motor, real-time compensation, torque ripple suppression.**

Nomenclature

$\mathbf{a}$	Torque characteristic vector.
$\mathbf{e}$	Unit-speed back-EMF vector.
$\mathbf{g}_i$, $\mathbf{g}_p$	Current and cogging torque harmonic vector.
$\mathbf{i}$, $\mathbf{i}_k$	Current harmonic amplitude vector and kth component.
$\mathbf{R}$, $\mathbf{L}$	Resistance and inductance matrices.
$\mathbf{u}$, $\mathbf{x}$	Control (voltage) and stator (current) vectors.
$\boldsymbol{\tau}_R$, $\boldsymbol{\tau}_{\text{cog}}$	Harmonic amplitude vectors of (ref., cog.) torque.
$\boldsymbol{\Gamma}$	Impedance vector of stator winding per phase.
a_j	jth component of a.
i_{mk}	kth harmonic amplitude of the mth phase current.
l_e	Effective length of the PM motor.
r_a	Mean radius of the air-gap.
r_{si}, r_{ro}	Stator-bore radius and rotor outer radii.
u_m, v_p	mth control voltage and the maximum voltage.
B_r, B_t	Radial and tangential components of net MFD.
B_{rE}, B_{tE}	(Radial, tangential) MFD components of windings.
B_{rP}, B_{tP}	Radial and tangential components of MFD by PMs.
L_S, M_S	Self- and mutual-inductance of phases.
N_{cog}	Number of cogging torque harmonic components.
N_k, N_τ	Number of current/torque harmonic components.
N_P, N_{ph}	Number of PM pole-pairs/phases.
N_S, N_t	Stator-slot number and wire-turns per coil.
R_S	Resistance of each phase.
T_{cog}	Cogging torque of the PM motor.
α_k	Phase angle of the kth current harmonic.
β_l	Phase angle of the lth cogging torque harmonic.
ϕ_m	Electrical phase angle of the mth phase.
μ_o	Permeability of air.
$\xi_{j\pm k}$	Harmonic indicator of torque ripples.
τ_c	Desired position-independent torque.
ω	Operating speed of the PM motor.
φ	Angular position in static-frame *XYZ*.
θ	Rotor displacement.

Manuscript received September 28, 2017; revised December 19, 2017 and January 22, 2018; accepted February 11, 2018. Date of publication February 23, 2018; date of current version June 26, 2018. This work was supported in part by U.S. National Science Foundation under Grant CMMI-1662700, and in part by the National Science Foundation of China under Grant 51675473 and Grant U1713204. The work of L. Li was supported by China Scholarship Council. *(Corresponding authors: Kok-Meng Lee; Kun Bai; Xiaoping Ouyang.)*

L. Li is with the State Key Laboratory of Fluid Power and Mechatronics Systems, Zhejiang University, Hangzhou 310027, China, and also with the Georgia Institute of Technology, Atlanta, GA 30332 USA (e-mail: tjull1991@163.com).

K.-M. Lee is with the State Key Laboratory of Digital Manufacturing Equipment and Technology, Huazhong University of Science and Technology, Wuhan 430074, China, and also with the Woodruff School of Mechanical Engineering, Georgia Institute of Technology, Atlanta, GA 30332 USA (e-mail: kokmeng.lee@me.gatech.edu).

K. Bai is also with the State Key Laboratory of Digital Manufacturing Equipment and Technology, Huazhong University of Science and Technology, Wuhan 430074, China (e-mail: kbai@hust.edu.cn).

X. Ouyang and H. Yang are with the State Key Laboratory of Fluid Power and Mechatronics Systems, Zhejiang University, Hangzhou 310027, China (e-mail: ouyangxp@zju.edu.cn; yhy@zju.edu.cn).

Color versions of one or more of the figures in this paper are available online at http://ieeexplore.ieee.org.

Digital Object Identifier 10.1109/TIE.2018.2808935

I. Introduction

MULTIPHASE permanent magnet (PM) motors have been increasingly used in emerging applications (for examples, more-electric aircraft [1]–[2], electric-vehicles [3], and intelligent manufacturing machines [4]) because of its intrinsic advantage in fault-tolerance and control performance [5]. Spin torque ripples (resulting from electromagnetic torque fluctuations and cogging torques) acting on the rotor incur vibrations and noises [6]. To ensure smooth and quiet operations of multiphase PM motors in high-performance applications, there is a need to develop effective design and control methods to suppress torque ripples. Although torque ripples can be suppressed by properly manipulating the multiphase currents, practical implementation in real time remains a challenge. A common problem is the lack of an appropriate inverse model that derives the desired currents and its effective solutions while avoiding any input-voltage saturation to control the multiphase PM motor in real time.

Techniques to suppress torque ripples of PM motors can be accommodated during the design stage (offline) and/or operation stage (online). For design purposes, a forward (torque) model that describes the effects of optimal parameters on the input currents and output torque is numerically analyzed for performance tradeoffs. Parametric investigations include the effects of PM shape [7]–[9] and arc [10], stator geometry [11], and slot/pole number combination [12] on torque ripples, where Sciuller [7] utilizes small trapezoid notches and [8] and [9] are based on harmonic injecting to optimize the PM shape to suppress the torque ripples. For a given PM motor design, the torque ripples can be further compensated through a real-time controller. A common method is to apply a direct torque controller that adjusts the control inputs based on the difference between reference and measured/estimated torques; for examples [13]– [15]. These methods require a flux estimator and a torque sensor with relatively high bandwidth and high resolution, and thus are generally costly in implementation.

Another common method is to derive a set of optimal input currents from an inverse model for a specified rotor displacement-independent torque at steady state, which are then used as a reference for feedback control of the phase currents. Inverse models for suppressing ripples can be classified into two categories depending on the formulation of the currents and torque ripples expressed in time domain or in terms of harmonics. Time-based inverse models [4], [12] derive the currents at each sampled rotor displacements. Harmonics-based inverse models compensate the torque-ripple harmonics with the phase-current harmonics (amplitudes and angles), which were calculated analytically [16], [17] or using artificial neuro-networks [18] for three-phase PM motors. However, the possible voltage saturation was not considered.

In practice, inverse models must be computed in real time; any reduction in computational time-delay can significantly improve the controller performance [19], [20]. Hence, it is essential to avoid complex algorithms (such as matrix inversion and iterations) when implementing the solutions to the inverse model in real time. As multiple solutions to the current inputs exist for a specified torque in multiphase PM motors, an optimal solution that minimizes a specified cost function (such as copper loss) is considered here. For a voltage-controlled multiphase PM motor operating at high speed [21], the input voltage inequality constraint poses another challenge for solving the optimal currents from the inverse model in real time. This paper proposes a method to formulate an inverse model in harmonic forms for deriving the desired currents to compensate the torque ripples in real time while minimizing copper losses; both with and without input-voltage saturations are considered. The remainder of this paper offers the following.

1) The torque model for a multiphase PM motor is formulated in harmonic forms, which provide a basis for analyzing the interactions between the harmonics of the torque/current gains and that of the input currents for compensating the torque-ripple harmonics using the current harmonics.
2) Two methods to derive the inverse models in harmonic forms are presented; a displacement-independent pseudo-inverse model for a multiphase motor without input saturation, and an iterative-free method to solve for an optimal current vector that minimizes its copper loss subject to the torque constraint and the voltage inequality constraint.
3) The formulation and physical significance of the proposed methods are illustrated with a multiphase PM motor where published measurements are available for model validation and benchmark comparison.

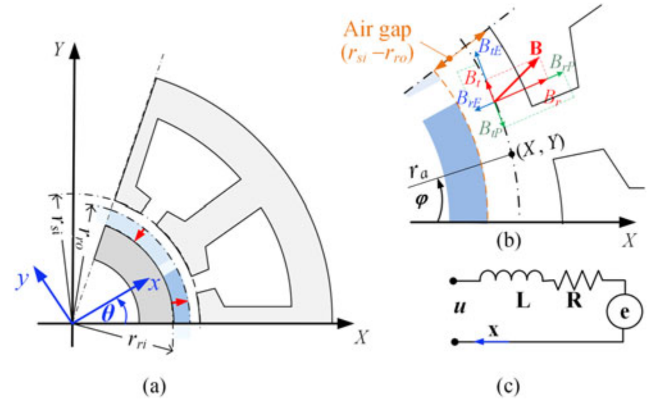

Fig. 1. Schematics illustrating multiphase PM motor. (a) Parameters used in model. (b) Air-gap MFD. (c) Equivalent stator winding circuit.

II. Inverse Models of a Multiphase PM Motor

Fig. 1(a) and (b) schematically shows the geometrical parameters for analyzing a multiphase PM motor, where the *XYZ* and *xyz* are the stator (reference) and rotor (moving) coordinate frames, respectively; the Z and z are aligned; and θ is the rotor displacement from the X-axis. In Fig. 1(b), φ denotes the angular position of a point in the air-gap between the rotor outer radius r_{ro} and the stator-bore radius r_{si} in the *XYZ* frame.

A. Analytical Models in State-Space Representation

The following assumptions are made in deriving the state-space models for control analysis of a multiphase PM motor.

1) The magnetic forces along X- and Y-axes are self-balanced and thus not considered in this study.
2) The N_P PM pole-pairs are surface-mounted on the cylindrical rotor iron-core (nonsalient). The spatial distribution of the PM remanences are symmetric about its center.
3) The stator windings are grouped into N_{ph} phases, each of which is constituted of N_C coils with N_t wire-turns such that the mth phase is characterized by the electrical angular position ϕ_m

$$\phi_m = \phi_1 + (m-1)\frac{2\pi}{N_{ph}} \text{ where } m = 1, \ldots, N_{ph}. \tag{1}$$

4) The effects of eddy-currents and the end-fringing on the magnetic flux density (MFD) in the stator/rotor air-gap are negligibly small [22]–[24].
5) The system with stator/rotor iron cores of infinitely large permeability and no iron-saturation is magnetically linear. Iron-saturation that results in degraded performances, is usually avoided during normal operations in industry, thus the assumption of no iron-saturation is reasonable.

1) Magnetic Field: At any stationary point $(r_{ro} \leq r \leq r_{si}, \varphi)$ within the air-gap, the net MFDs contributed by the PMs and the currents flowing through the stator windings can be decomposed into radial and tangential components (B_r, B_t)

$$\mathbf{B} = \begin{bmatrix} B_r \\ B_t \end{bmatrix} = \begin{bmatrix} B_{rP} + B_{rE} \\ B_{tP} + B_{tE} \end{bmatrix}. \quad (2)$$

In (2), the subscripts "*P* and *E*" denote that the MFDs contributed by the rotor-PMs and the electrical stator windings, respectively. For completeness, the formulation based on exact subdomain model [22]–[24] for computing (B_r, B_t) is given in Appendix A, which provides a basis to solve for the back electromotive force (EMF) and the electromagnetic torque.

2) Electrical Circuit Model: Fig. 1(c) shows an equivalent RL circuit for lumped-parameter modeling of the electrical input system to the motor, where (**u**, **e**) are the (input voltage, unit-speed back-EMF); and (**R**, **L**) are the (resistance, inductance) matrices made up of the phase resistance R_S,, self-inductance L_S, and mutual-inductance M_S. The phase currents (i_m where $m = 1, 2 \ldots N_{ph}$) are described by the column vector $\mathbf{x}(\theta)$ defined in (3)

$$\mathbf{x}(\theta) = \left[i_1(\theta) \cdots \quad i_m(\theta) \cdots \quad i_{N_{ph}}(\theta) \right]^{\mathrm{T}}. \quad (3)$$

In state-space representation, the phase-current vector **x** is governed by the control (voltage) vector **u** and unit-speed back-EMF vector **e** (that depends on the rotor displacement θ)

$$\mathbf{u} = \mathbf{L}\frac{d\mathbf{x}}{dt} + \mathbf{R}\mathbf{x} + \omega\,\mathbf{e}(\theta) \quad (4a)$$

$$\mathbf{R} = \mathrm{diag}\left(R_S \cdots \quad R_S \cdots \quad R_S \right) \quad (4b)$$

$$\text{and} \quad \mathbf{L} = \begin{bmatrix} L_S & M_S & \ldots & M_S \\ M_S & L_S & \ldots & M_S \\ \cdots & \cdots & \cdots & \cdots \\ M_S & M_S & M_S & L_S \end{bmatrix}. \quad (4c)$$

In (4a), $\omega = \mathrm{d}\theta/\mathrm{d}t$ is the PM motor operating speed; and **u** and **e** are the column vectors with elements u_m and e_m, respectively, where $m = 1, 2, \ldots, N_{ph}$.

3) Torque Model: The electromagnetic torque $\tau(\theta)$ of the multiphase PM motor can be derived using the Maxwell stress tensor [22]

$$\tau(\theta) = \frac{l_e r_a^2}{\mu_o} \int_0^{2\pi} [B_{rE} B_{tE} + (B_{rE} B_{tP} + B_{rP} B_{tE}) + B_{rP} B_{tP}]\, d\varphi. \quad (5a)$$

For motors with nonsalient rotor-cores, $B_{rE} B_{tE}$ does not contribute to the generation of the torque. Hence, the torque can be expressed as

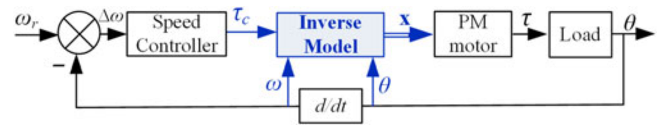

Fig. 2. Inverse model in the speed control system for PM motors.

$$\tau(\theta) = \mathbf{a}\mathbf{x} + T_{\mathrm{cog}}(\theta) \quad (5b)$$

where $r_a = (r_{ro} + r_{si})/2$ is the mean radius of the air-gap. The 1st term on the right side of the forward model (5b) can also be computed using the Lorentz-force equation, where the torque/current gain **a** is a row vector of N_{ph} elements, $a_m(\theta, \phi_m)$. The cogging torque T_{cog} depends on $B_{rp} B_{tp}$ of the PMs. For low-loss motors, $\mathbf{a} \approx \mathbf{e}^T$ [18]. To generate a ripple-free torque of the PM motor, torque ripples (originated from T_{cog} as well as the interactions between **e** and **x**) must be suppressed.

B. Inverse Models

For a multiphase motor where the number of independent inputs is larger than one (single-axis rotating motor), an optimum **x** that minimizes a cost function for a specified position-independent τ_c at steady-state can be formulated as the inverse model. Unlike the forward model (5b) where $\tau(\theta)$ is uniquely solved in terms of **x** for design and offline analysis, the inverse model must be computed in real time for the phase-current vector **x** for varying τ_c to eliminate the speed error $\Delta\omega$ between the speed reference ω_r and ω in the speed control system as shown in Fig. 2.

1) Time Domain Inverse Model: For generating a position-independent τ_c at steady-state, a common inverse model is given in (6) where the optimal **x** is derived from the pseudo-inverse of $\mathbf{a}(\theta)$ that minimizes the copper loss of a current-controlled ironless PM motor

$$\mathbf{x} = \mathbf{a}(\theta)\left[\mathbf{a}(\theta)\mathbf{a}^{\mathrm{T}}(\theta)\right]^{-1} [\tau_c - T_{\mathrm{cog}}(\theta)]. \quad (6)$$

Once the optimal **x** is found, the control vector **u** can be determined from (4a). However, **x** in (6) depends on the rotor displacement θ and thus, additional memory is required to store the look-up table of $\mathbf{a}(\theta)$. For a multiphase PM motor (with large N_{ph}) operating at high speed, the real-time computational update of the displacement-dependent current vector $\mathbf{x}(\theta)$ from (6) that neglects input saturation presents a significant problem in implementing the optimal torque control in practice.

2) Inverse Model in Harmonic Form (Without Input Voltage Constraint): Because of the periodicity, (i_m, T_{cog}, and τ) can be expressed in harmonic forms [25]. The method, which takes advantages of the forward model to reduce computation in real time, identifies the phase current harmonics for suppressing the torque ripples. In this method, the mth phase of the current vector $\mathbf{x}(\theta)$ is expressed in terms of the parameter vectors ($\mathbf{g}_i$ and **i**) to characterize the identified current harmonics

$$i_m(\theta) = \mathbf{g}_i(\theta)\mathbf{i}. \quad (7a)$$

In practice, only finite N_k current harmonic components are considered; $\mathbf{g}_i \in \mathbb{R}^{1\times 2N_k}$ and $\mathbf{i} \in \mathbb{R}^{2N_k\times 1}$. Similarly, the cogging torque T_{cog} can be rewritten as

$$T_{\text{cog}}(\theta) = \mathbf{g}_p(\theta)\tau_{\text{cog}}. \quad (7b)$$

With (7a) and (7b), an alternative displacement-independent pseudo-inverse model (8) for a multiphase PM motor *without input saturation* can be derived to generate the specified position-independent τ_c while eliminating the torque ripples due to $T_{\text{cog}}(\theta)$

$$\mathbf{i} = \mathbf{Z}\left[\mathbf{Z}\mathbf{Z}^{\mathrm{T}}\right]^{-1}\boldsymbol{\tau}_R \quad \text{where } \boldsymbol{\tau}_R = \left[\tau_c \ -\boldsymbol{\tau}_{\text{cog}}^{\mathrm{T}}\right]^{\mathrm{T}}. \quad (8)$$

Given that N_{cog} harmonic components of the cogging torque T_{cog} are significant, the motor torque τ must have N_τ harmonic components to eliminate the ripples while avoiding undesired harmonics caused by the interactions between $\mathbf{a}(\theta)$ and $\mathbf{x}$

$$\boldsymbol{\tau}_R \in \mathbb{R}^{(2N_\tau+1)\times 1} \text{ where } N_{\text{cog}} \le N_\tau < N_k.$$

The vectors $(\mathbf{g}_i,\, \mathbf{g}_p,\, \boldsymbol{\tau}_{\text{cog}})$ and matrix $\mathbf{Z}$ in (8) are derived in the Section II-C from the harmonic-based forward torque model for offline computation.

C. Harmonic Components in Torque Model

In harmonic forms (with period $2\pi/N_P$), the mth element of the vectors $\mathbf{a}(\theta)$ and the current i_m of a typical multiphase PM motor are given by (9a) and (9b), respectively

$$a_m(\theta, \phi_m) = \sum_{j=1,3,5\ldots}^{\infty} a_j \sin(j\theta_m) \quad (9a)$$

$$i_m(\theta) = \sum_{k=1,3,5\ldots}^{\infty} i_{mk} \sin(k\theta_m + \alpha_k). \quad (9b)$$

In (9a) and (9b), (a_j, i_{mk}) are the $(j, k)^{\text{th}}$ harmonic amplitudes of (a_m, i_m); $\theta_m = N_P\theta - \phi_m$ and α_k is the corresponding angle difference from θ_m. Similarly, the harmonic form of the cogging torque model is given in (9c) where (τ_l, β_l) are the (amplitude, phase angle) of its lth harmonics and N_r is the least common multiple of the slot number N_S and $2N_P$ [11]

$$T_{\text{cog}}(\theta) = \sum_{l=1,2,3\ldots}^{\infty} \tau_l \sin(lN_r\theta + \beta_l). \quad (9c)$$

1) Position-Dependent Torque Model:

From (9b) and (9c), the components of the phase current i_m and the cogging torque defined in (7a) and (7b) are derived as follows:

$$\mathbf{i}^{\mathrm{T}} = \left[\ldots \ \ \mathbf{i}_k \ \ \ldots\right] \quad (10a)$$

$$\text{where } \mathbf{i}_k = i_{mk}\mathbf{h}'(\alpha_k) \quad (10b)$$

$$\text{and } \mathbf{g}_i(\theta) = \left[\ldots \ \ \mathbf{h}(k\theta_m) \ \ \ldots\right] \quad (10c)$$

$$\boldsymbol{\tau}_{\text{cog}}^{T} = \left[\ldots \ \ \tau_l \mathbf{h}(\beta_l) \ \ \ldots\right] \quad (11a)$$

$$\text{and } \mathbf{g}_p(\theta) = \left[\ldots \ \ \mathbf{h}'(lN_r\theta) \ \ \ldots\right] \quad (11b)$$

$$\text{where } \mathbf{h}(\cdot) = \left[\sin(\cdot) \ \ \cos(\cdot)\right] \quad (12a)$$

$$\text{and } \mathbf{h}'(\cdot) = \left[\cos(\cdot) \ \ \sin(\cdot)\right]. \quad (12b)$$

Since all the phase currents (i_m where $m = 1,\ldots,N_{ph}$) and their corresponding kth harmonic components have the same amplitude i_{mk} phase difference angle α_k, the forward model (5b) for generating a steady-state τ_c is rewritten in harmonic forms using (9a) and (9b) and the derivation is given in Appendix B

$$\tau_c - T_{\text{cog}}(\theta) = \mathbf{a}(\theta)\mathbf{x} = \sum_{k=1,3..}^{\infty}\left(\sum_{j=1,3\ldots}^{\infty}\left[\mathbf{h}'(\theta_{j-k}) \ \ \mathbf{h}'(\theta_{j+k})\right] \times \begin{bmatrix}\mathbf{Z}_{j-k}\\ \mathbf{Z}_{j+k}\end{bmatrix}\right)\mathbf{i}_k \quad (13a)$$

$$\text{where } \mathbf{Z}_{j\pm k} = \frac{N_{ph}a_j\xi_{j\pm k}}{2}\begin{bmatrix}\mp 1 & 0\\ 0 & \operatorname{sgn}(j\pm k)\end{bmatrix} \quad (13b)$$

$$\theta_{j\pm k} = (j\pm k)(N_P\theta - \phi_1) \quad (13c)$$

$$\text{and } \xi_{j\pm k} = \begin{cases}1 & j\pm k = \ell N_{ph},\ \ell = 0, \pm 1, \ldots\\ 0 & \text{others}\end{cases}. \quad (13d)$$

In (13a), $\mathbf{h}'(\theta_{j\pm k})$ defined in (12b) and (13c) depends on θ accounting for the phase angle of the $(j \pm k)$th components of the Lorentz force harmonics (due to the interaction between $\mathbf{a}$ and $\mathbf{x}$) for a given N_P. On the other hand, the coefficient matrix $\mathbf{Z}_{j\pm k}$ defined in (13b) depends only on its amplitude $a_j\xi_{j\pm k}/2$ for a given N_{ph} where $\xi_{j\pm k}$ serves as a harmonic indicator. The term sgn($j-k$) is used to negate $\theta_{j\pm k}$ when $j < k$.

2) Position-Independent Ripple-Free Torque Model:

For solving the optimal currents (8), (13a) is rewritten as (14a) to identify the position-independent τ_c

$$\mathbf{Z}\mathbf{i} = \begin{bmatrix}\mathbf{z}_c\\ \mathbf{Z}_c\end{bmatrix}\mathbf{i} = \boldsymbol{\tau}_R. \quad (14a)$$

As shown in (13a) and (13c), $\theta_{j-k} = 0$ and $\mathbf{h}'(0)\mathbf{Z}_{j-k} = (N_{ph}a_j/2)$ [1 0] when $j = k$. The ripple-free torque τ_c can be formulated as

$$\tau_c = \frac{N_{ph}}{2}\sum_{k=1,3\ldots}^{\infty}\left[a_{j=k}\mathbf{h}'(0)\right]\mathbf{i}_k = \mathbf{z}_c\mathbf{i} \quad (14b)$$

$$\text{where } \mathbf{z}_c\left(\in \mathbb{R}^{1\times 2N_k}\right) = \frac{N_{ph}}{2}\left[a_1\mathbf{h}'(0)\cdots \ a_{j=k}\mathbf{h}'(0) \ \cdots\right]. \quad (14c)$$

From (14a), $\boldsymbol{Z}_c\boldsymbol{i} = -\boldsymbol{\tau}_{\text{cog}}$; thus, $\boldsymbol{Z}_c$ has the following form:

$$\mathbf{Z}_c\left(\in \mathbb{R}^{2N_\tau\times 2N_k}\right) = \begin{bmatrix}\mathbf{Z}_{l1}\cdots & \mathbf{Z}_{lk} & \cdots\\ \vdots\cdots & \vdots & \cdots\vdots\\ \mathbf{Z}_{l1}\cdots & \mathbf{Z}_{lk} & \cdots\\ \vdots\cdots & \vdots & \cdots\vdots\end{bmatrix} \quad (14d)$$

$$\text{where } \mathbf{Z}_{lk}\left(\in \mathbb{R}^{2\times 2}\right) = \sum_{|j\pm k|N_P = \ell N_r}(\mathbf{Z}_{j-k} + \mathbf{Z}_{j+k}). \quad (14e)$$

The $\mathbf{Z}$ formulated in (14) is position-independent providing a basis to precompute the optimal $\mathbf{i}$ and phase current i_m from (8) and (7a), respectively, for a specified $\boldsymbol{\tau}_R$. The solutions to

(3) based on (8) assumes that none of the input voltage element u_m in (4a) is saturated.

D. Inverse Model With Input Voltage Constraint

For a multiphase PM motor with symmetrical components, the sum of i_m (where $m = 1, \ldots, N_{ph}$) is zero. The mth element of the control vector in (4a) is given by

$$u_m = (L_S - M_S)\,\omega \frac{d\mathbf{g}_i(\theta)}{d\theta}\mathbf{i} + R_S \mathbf{g}_i(\theta)\mathbf{i} + \omega e_m.$$

Given that each phase control-voltage u_m is bounded by the maximum available voltage $|v_p|$, the constraint equation can be written as (15) where $\mathbf{h}$ is defined in (12a)

$$|u_m| = \omega\,|\mathbf{\Gamma}(\theta_m)\,\mathbf{i} + e_m(\theta)| \le |\nu_p| \tag{15}$$

where $\mathbf{\Gamma}(\theta_m) = \left[\ldots \left[(L_S - M_S)\frac{d}{d\theta} + \frac{R_S}{\omega}\right]\mathbf{h}(k\theta_m)\ldots\right]$.

In the following discussion, the impedance vector $\mathbf{\Gamma}(\theta_m)$ and back-EMF $e_m(\theta)$ are assumed to have the same waveform but different phase angles defined in (9b); thus, all the N_{ph} phases have the maximum $|u_m|$.

To account for any phase input voltage saturation, the inverse model is formulated as an optimization problem that minimizes the copper loss $J(\mathbf{i})$ subject to the torque and input constraints

$$J(\mathbf{i}) = \frac{1}{2}R_S \sum_{m=1}^{N_{ph}} \int_{\theta_i}^{\theta_i + 2\pi/N_P} [\mathbf{g}_i(\theta)\mathbf{i}]^2\, d\theta.$$

Mathematically, the optimal $\mathbf{i}$ is solved from the following equations:

$$\text{Minimize}\quad J(\mathbf{i}) = \frac{\pi}{2}\left(\frac{N_{ph}}{N_P}\right) R_S \mathbf{i}^T\mathbf{i} \tag{16a}$$

$$\text{Subject to}\quad \mathbf{Z}\mathbf{i} = \boldsymbol{\tau}_R \tag{16b}$$

$$\text{and}\quad |\mathbf{\Gamma}(\theta)\mathbf{i} + e_m(\theta)| \le \frac{|\nu_p|}{\omega}. \tag{16c}$$

To solve the inverse model with *input saturation*, the number of current harmonics N_k should be larger than N_τ by 1 such that the dimension of $\mathbf{i}\,(2N_k)$ is larger than the equality constraints number $(2N_\tau + 1)$ in (16b) by 1. Equation (16b) can be rewritten as

$$\frac{\boldsymbol{\tau}_R}{i_{m1}\cos\alpha_1} - \sum_{i=3,5\ldots}^{N_k}\left[\mathbf{Z}_i\ \mathbf{Z}_{i+1}\right]\frac{\mathbf{i}_k^{\mathrm{T}}}{i_{m1}\cos\alpha_1} = \mathbf{Z}_1 + \mathbf{Z}_2\tan(\alpha_1)$$

that can be reduced to the form in the following equation:

$$\mathbf{i}' = \left[\tau_R \quad \ldots \quad \mathbf{Z}_i \quad \mathbf{Z}_{i+1} \quad \ldots\right]^{-1}\left[\mathbf{Z}_1 + \mathbf{Z}_2\tan(\alpha_1)\right] \tag{17}$$

where $\mathbf{i}' = \frac{1}{i_{m1}\cos\alpha_1}[1 \cdots \mathbf{i}_k \cdots]^T$; $\mathbf{Z}_i$ is the ith column vector of $\mathbf{Z}$ defined in (14a); and $\mathbf{i}_k$ corresponds to the $(0.5i + 0.5)$th subvector of $\mathbf{i}$. Given $(\mathbf{Z}, \tau_R)$, (17) implies that $\mathbf{i}_k (k = 3, \ldots)$ and $i_{m1}\cos\alpha_1$ can be expressed in terms of $(\tan\alpha_1)$; thus (16a) and (16c) depend only on $(\tan\alpha_1)$. From (14c), the 1st element of $\mathbf{Z}_2$ is 0; hence $i_{m1}\cos\alpha_1$ is invariant with $(\tan\alpha_1)$. Furthermore, the cost function (16a) is proportional to the fundamental component and increases with $|\tan\alpha_1|$,

$$\mathbf{i}_1^T\mathbf{i}_1 = (i_{m1}\cos\alpha_1)^2\left(1 + \tan^2\alpha_1\right).$$

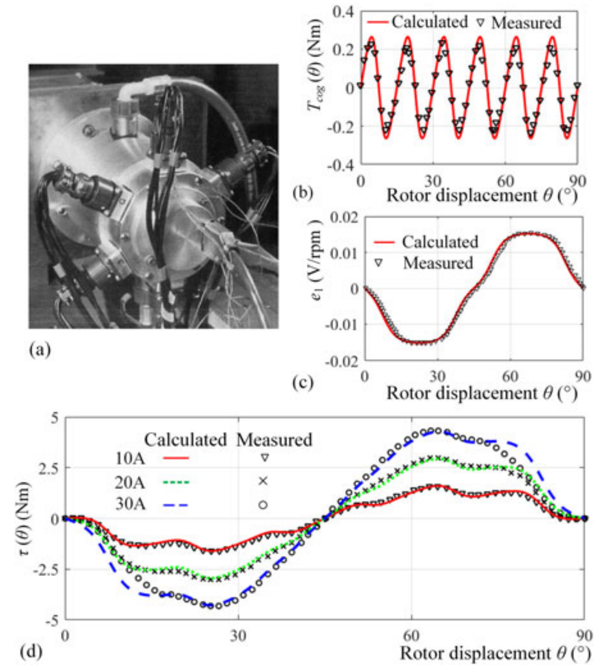

Fig. 3. Forward model validation. (a) PM motor prototype [2], [26]. (b) Cogging torque T_{cog}. (c) Phase 1 back-EMF. (d) Torque τ.

Thus, the optimal solutions to (16) correspond to the minimum $|\tan\alpha_1|$ that satisfies the inequality constraint (16c).

Given $\mathbf{\Gamma}(\theta_m)$ and $e_m(\theta)$, the maximum $|u_m/\omega|$ as a function of $\mathbf{i}$ (that depends on τ_c and/or $\tan\alpha_1$) can be calculated offline from (8) and (15) in advance to determines whether the input voltage is saturated or the voltage constraint (16c) is violated. To account for the input voltage constraint, $\mathbf{i}'$ in (17) is computed as a function of $(\tan\alpha_1)$ for a specified τ_c, which are then substituted into (15) to compute the maximum $|u_m|/\omega$. The minimum $|tan\,\alpha_1|$ that satisfies (16c) is stored as a two-dimensional (2-D) look-up table output with τ_c and $|v_p|/\omega$ as inputs to determine the optimal $(\tan\alpha_1)$ in real time. With the optimal $(\tan\alpha_1)$, $\mathbf{i}$ can be directly solved from (17). This iteration-free method represents a novel improvement over traditional solutions to an optimization problem with inequality constraints.

In summary, $(\mathbf{Z}, \mathbf{i}, \text{and}\, \boldsymbol{\tau}_{\text{cog}})$ formulated in the position-independent torque model (14a)–(14e) can be predetermined. For operations without any input constraints, the optimal currents are given by (8). For operations with input constraints (16c), a look-up-table that stores the optimal $(\tan\alpha_1)$ for specified τ_c and $|v_p/\omega|$ is used to derive the optimal currents from (17).

III. Results and Discussions

The formulation and physical significance of the inverse models are illustrated with the multiphase PM motor [see Fig. 3(a)] reported in [2], [26] where essential parametric values (listed in the top right of Table I) and experimental measurements are available for model validation and benchmark comparison. The PM motor was designed with a rated sinusoidal current $I_n = 21.1$ A (rms value) and dc link voltage 270 V. To provide a basis for illustration, the solutions to the forward model (5b)

TABLE I
MAIN PARAMETRIC VALUES OF THE PM MOTOR

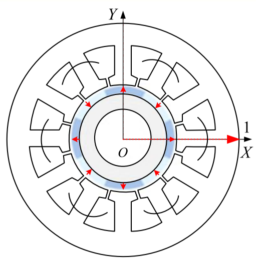

	Windings: N_t =50, N_C =1, N_S=12. R_S=0.156Ω, L_S=1.275mH v_p = 270V, I_n=21.1A **PM:** (Parallel magnetized): arc θ_p=45°, thickness l_m=8mm **Stator:** l_e=80mm, r_{si}=27.5mm **Rotor:** r_{ri}=17.5mm, r_{ro}=25.5mm, ϕ_1=0°
	N_l=2, N_r =LCM(N_S, N_P) = 24 a_1=−0.1407; a_5=0.0084; a_7=0.0028 τ_1=0.255, τ_2=−0.042, β_1=β_2=0

TABLE II
HARMONICS IDENTIFICATION (N_{ph} = 6 AND N_P = 4)

	$k=1$	$k=3$	$k=5$	$k=7$	$k=9$	$k=11$
$j=1$	**0**	0	(24)	(24)	0	48
$j=3$	0	**0, 24**	0	0	24, 48	0
$j=5$	(24)	0	**0**	(48)	0	24
$j=7$	(24)	0	(48)	**0**	0	72
$j=9$	0	24, 48	0	0	**0, 72**	0
$j=11$	48	0	24	72	0	**0**

based on the scalar magnetic potentials formulated in Appendix A are analytically calculated and verified against published measurements [26] in Fig. 3.

The following observations can be made from Fig. 3.

1) Fig. 3(b) and (c) shows good agreements between the computed cogging torque $T_{\text{cog}}(\theta)$ and the (Phase 1) non-sinusoidal unit-speed back-EMF $e_1(\theta)$ and the published measurements.
2) Fig. 3(d) shows the computed torque $\tau(\theta)$ generated with a constant (Phase 1) current, where the results for three different current values (10, 20, and 30 A) are compared with the measured torques. The torque comparisons agree excellently well except in the regions ($\theta \in$ [0°, 20°]∪ [70°, 90°]) when Phase 1 was supplied with constant 30 A. The discrepancy was caused by the magnetic saturation occurred in the stator-iron where both $(B_{rP},\ B_{tP})$ and $(B_{rE},\ B_{tE})$ are relatively large and in same direction.
3) The comparisons validate the forward model (5b) of the PM motor (without stator-iron saturation) for formulating (14a) and solving the inverse model (8). In general, constant exciting currents are only used for test purpose and the iron saturation can be avoided by proper manipulating the phase current angle α_1 of the fundamental component.

The remaining results are organized into three sections: Section III-A illustrates the formulation of the forward model (14a) of the PM motor (without stator-iron saturation) for solving the inverse model (8). The effects of the input-voltage saturation on the torque ripples and copper losses are discussed in Section III-B. In Section III-C, the inverse models are validated by comparing the harmonics-based inverse solutions with published experimental data [26] and evaluated against the time-based inverse model (6).

A. Inverse Model (Without Input Constraint)

As indicated in Table I, Phase 1 is located at $\phi_1 = 0$ deg. The stator windings are singer-layered with negligible mutual inductance ($M_S \approx 0$ mH as compared with the individual self-inductance [27]). Using (9a) and (9c), the torque/current gain and the cogging torque T_{cog} were determined analytically in (18a) and (18b) where the coefficients are listed in Table I (bottom right)

$$a_m\ (\approx e_m) \approx a_1 \sin\theta_m + a_5 \sin 5\theta_m + a_7 \sin 7\theta_m \quad (18a)$$

$$T_{\text{cog}}(\theta) \approx \tau_1 \sin(N_r\theta + \beta_1) + \tau_2 \sin(2N_r\theta + \beta_2). \quad (18b)$$

The forward model (14a) of the PM motor for solving the inverse model (8) in harmonic forms is formulated as follows:

Step 1: identifies the torque harmonics contributed by $\mathbf{a}(\theta)\mathbf{x}$ using (13b). The results (for $j,\, k = 1, 3, 5, 7, 9, 11$) are tabulated in Table II to facilitate the discussion. The diagonal ($j = k$) elements are $\theta_{j\pm k} = (\mathbf{0}, 2kN_P\theta)$ where the bold zeros imply that the torque components are ripple-free. The nonzero element (when $j \pm k = \ell N_{ph}$) results in a nonzero $\mathbf{Z}_{lk}$ in (14e) with $\theta_{j\pm k} = 24\,\theta, 48\,\theta, 72\,\theta$.

Step 2: determines the k orders of current harmonics. As shown in (18a) and (18b), j = 1,5,7 and $l = 1, 2$. Since $N_\tau \geq N_{\text{cog}} = 2$ and $lN_r = (24, 48)$, the torque due to the interactions between $\mathbf{a}(\theta)$ and $\mathbf{x}$ must be capable of compensating the cogging torque ripples with harmonics $\theta_{j\pm k} = (24\,\theta, 48\,\theta)$ while avoiding $(j \pm k)N_P = 72$ that introduces an unwanted harmonics $\theta_{j\pm k} = 72\theta$. As illustrated in Table II, the $k\ (= 1, 5, 7)$ current harmonics would produce the same T_{cog} harmonic components. Thus, $(\mathbf{i},\ \boldsymbol{\tau}_{\text{R}})$ can be formulated as

$$\mathbf{i} = \begin{bmatrix} \mathbf{i}_1 & \mathbf{i}_5 & \mathbf{i}_7 \end{bmatrix}^{\text{T}} \quad (19a)$$

$$\text{and } \boldsymbol{\tau}_R = \begin{bmatrix} \tau_c & -\boldsymbol{\tau}_1\mathbf{h}(\beta_1) & -\boldsymbol{\tau}_2\mathbf{h}(\boldsymbol{\beta_2}) \end{bmatrix}. \quad (19b)$$

Step 3: formulates $\mathbf{z}_c$ and $\mathbf{Z}_c$ according to (14b), (14c) and (14d), (14e)

$$\mathbf{z}_c = \frac{N_{ph}}{2} \begin{bmatrix} a_1 & 0 & a_5 & 0 & a_7 & 0 \end{bmatrix} \quad (19c)$$

$$\mathbf{Z}_c = \begin{bmatrix} \mathbf{Z}_{7-1} + \mathbf{Z}_{5+1} & \mathbf{Z}_{1+5} & \mathbf{Z}_{1-7} \\ \mathbf{0}_{2\times 2} & \mathbf{Z}_{7+5} & \mathbf{Z}_{5+7} \end{bmatrix}. \quad (19d)$$

B. Inverse Model Accounting for Input Saturation

Fig. 4(a) and (b) shows the maximum-voltage to operating-speed ratio u_a/ω against the specified torque and ($\tan\alpha_1$) for the PM motor (see Table I), respectively. Fig. 4(a) was computed based on (8) and (15). To account for the input voltage constraint for high-speed operations (where R_S/ω can be neglected as compared with inductive impedance), $i_{m1}\cos\alpha_1$ and $\mathbf{i}'_k$ are computed as a function of ($\tan\alpha_1$) from (17) and substituted into (15) to compute $|u_m|/\omega$ for known $\boldsymbol{\Gamma}(\theta_m)$ and $e_m(\theta)$. As shown in Fig. 4(b), u_a/ω linearly decreases with ($\tan\alpha_1$) until a minimum point beyond which the effects induced by increased α_1 are cancelled by the increase of i_{m1}. To avoid the extremely large amplitude of i_{m1}, only the zone of decreasing

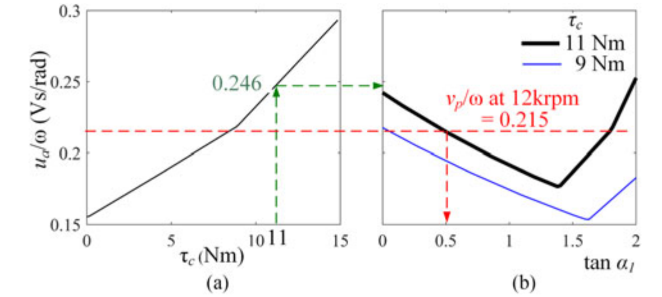

Fig. 4. Maximum-voltage to operating-speed ratio. (a) Function of τ_c. (b) Function of (tan α_1).

u_a/ω is precomputed and stored as a look-up table; the linear relationship greatly reduces the memory needed. Once (tan α_1) is determined from Fig. 4(b), the optimal **i** can be directly derived from (17).

As an illustration, consider the operating conditions ($\tau_c = 9, 11\,\mathrm{N \cdot m}$ at $\omega = 4, 12\,\mathrm{kr/min}$; the latter corresponding to $v_p/\omega = 0.645$ and 0.215 Vs/rad, respectively. From Fig. 4(a), $\tau_c = 9$ and 11 N·m would call for $u_a/\omega = 0.21$ and 0.246, respectively. For $\tau_c = 9\,\mathrm{N \cdot m}$ at $\omega = 4, 12\,\mathrm{kr/min}$, no input saturation is expected as $u_a/\omega < v_p/\omega$. Similarly, the case ($\tau_c = 11\,\mathrm{N \cdot m}$ at $\omega = 4\,\mathrm{kr/min}$) will have no input saturation since $u_a/\omega < v_p/\omega$. However, u_a/ω (=0.246 Vs/ rad) would exceed the allowable control voltage v_p of 270 V (or $v_p/\omega = 0.215$ Vs/ rad) when operating at a high speed of 12 kr/min (while maintaining the same τ_c of 11 N·m). As illustrated in Fig. 4(b) where the red dashed-line indicates the allowable v_p/ω at 12 kr/min, the corresponding (tan α_1) is determined to be 0.5.

C. Validation and Evaluation of the Inverse Models

The effectiveness of the inverse models is evaluated by comparing computed results with published experimental data [26] where the PM motor was operated at the speed of 4 kr/min with average torque around 11 N·m. In addition to computation time T_c, two other performance indexes (torque-ripple rate δ_τ and copper loss rate η) defined in the following equations are used:

$$\delta_\tau = \frac{\tau - \bar{\tau}}{\bar{\tau}} \times 100\% \tag{20a}$$

$$\text{and} \quad \eta = \frac{J}{\bar{\tau}\omega} \times 100\% \tag{20b}$$

1) *Sinusoidal current inputs* (SI)*:* The PM motor is excited with sinusoidal current; only i_{m1} is supplied.
2) *Back-EMF shapes* (BE)*:* (18a) where $\alpha_k = 0$ for $k = 1, 5, 7$. Results are presented in Table III and Fig. 4.
3) *Time-based inverse model* (TI), (6).
4) *Harmonics-based inverse model* (HI), (7a) and (8).
5) *Harmonics-based optimization* (HO), (16).

The results are summarized in Table III, Fig. 5 for SI and BE and Fig. 6 for TI, HI, and HO.

The following are some findings drawn from the comparisons in Table III, Figs. 5 and 6.

TABLE III
PERFORMANCE COMPARISON

	$(i_{m\,k}, \alpha_k)$, $k = 1, 5, 7, 11$. Unit: (A, °)	δ_τ (%)	η (%)	T_c (ms)
SI	(−25.8, 0), (0, 0), (0, 0), (0, 0)	±4.6	6.85	
BE	(−26.6, 0) (1.6, 0) (0.53, 0) (0, 0)	±8.4	7.01	
TI	(−26, 0) (0.6, −6) (1.58, 1.5) (0.17, −12.2)	0	6.86	1.48
HI	(−26.1, 0.15) (1.88, 115) (1.14, 76.8) (0,0)	±0.18	6.94	0.025
HO	(−29.2, 26.5) (1.2, 130) (1.2, 79) (0,0)	±0.18	8.63	0.073

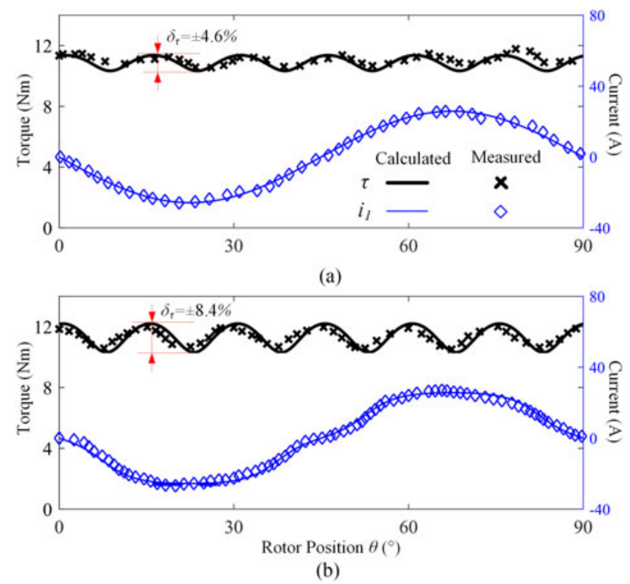

Fig. 5. Current waveforms and the resulting torque ripples. (a) Sinusoidal. (b) Back-EMF.

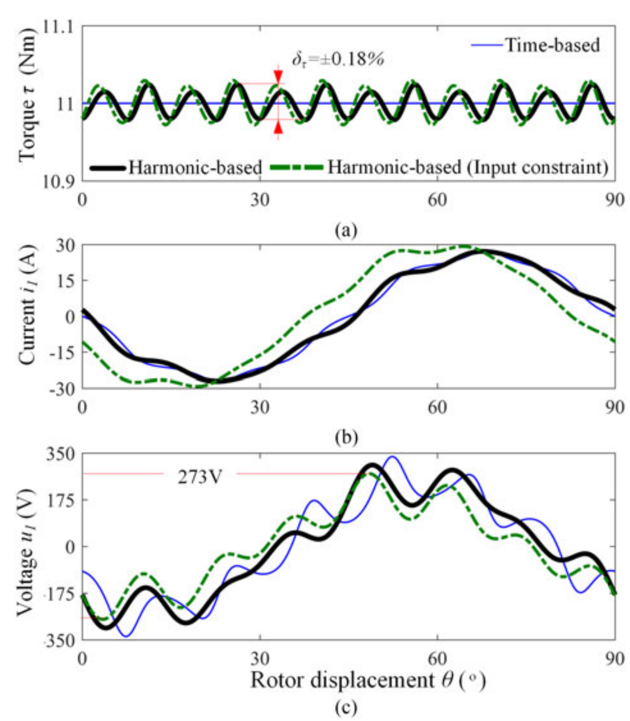

Fig. 6. Time- and harmonics-based inverse models. (a) The resulting torque. (b) Phase 1 current. (c) Phase 1 voltage at 12 kpm.

1) As compared with SI and BE (with ±4.6% and ±8.4% ripples, respectively), Table III shows that the three inverse models are capable of compensating the torque ripples. The time-based inverse model (6) theoretically yields a ripple-free torque ($\tau_c = 11\,\mathrm{N{\cdot}m}$) that provides a basis for comparison. As compared in Fig. 6(a), the close agreement with the time-based invers model (within ±0.2% of the mean torque) validates the harmonics-based inverse model. The slight discrepancy is due to the approximation in (18a) and (18b) where higher-order harmonics were neglected.
2) From Fig. 5(a) and (b), BE contains more current harmonics than SI but generates larger torque ripples ($\delta_\tau = \pm 8.4\%$) than SI ($\delta_\tau = \pm 4.6\%$). This can be explained with the aid of Table II that shows the torque harmonic components (24θ, 48θ) contributed by the interactions of a_j and i_{mk} ($j, k = 1, 5, 7$). Since the angles of current harmonics are not considered in both SI and BE, the adverse effects of the torque ripples increase with the number of uncontrolled harmonic interactions (between a_j and i_{mk}). This explains why BE ripples are more pronounced than SI that involves only the fundamental current component i_{m1}.
3) Unlike BE where $\alpha_k = 0$, the current harmonics (both amplitudes and angles) are identified in HI (19a) and formulated (19b)–(19d) for compensating the corresponding torque ripple harmonics. As shown in Table III where the computation times for the inverse solutions (based on a PC with 2.3 GHz and 16 G memory) are compared, the harmonic-based solutions (HI and HO) requiring no matrix inversions take much less time than the time-based solutions, 2% and 5% corresponding to HI and HO, respectively.
4) Except HO where the phase angle α_1 is advanced to keep the input voltage within the allowable limits, all four current waveforms result in similar copper loss of approximately 6.9%. Since the cost function increases with $(\tan\alpha_1)^2$, the larger copper loss in HO (that relaxes the no saturation assumption made in TI and HI) can be viewed as a cost to prevent input saturation.

IV. Conclusion

The methods to formulate the forward and inverse models of multiphase PM motors for identifying the harmonic components for eliminating torque ripples were presented in this paper. The formulation and the physical significance of the inverse models were illustrated with a typical PM motor. The methods were evaluated in terms of torque ripples, computational time and copper loss by comparing published experimental data and three other commonly used current waveforms. As compared with the commonly used time-based inverse model, input-voltage saturation causing current distortions can be overcome; and large torque ripples can be suppressed within ±0.2% of the mean torque by the harmonics-based inverse model that takes less than 80 μs to compute an update. These findings confirm that the proposed inverse model and its time-efficient solutions provide a practical means to suppress torque ripples in a PM motor, and can be implemented in its real-time control systems for high-speed operations. Further work will focus on extending the harmonic-based inverse models to more general applications; for example, multiphase PM motor subjected to unbalanced forces.

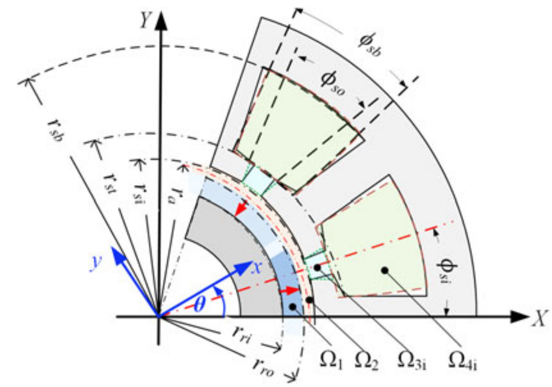

Fig. 7. Parameters used in subdomain model.

TABLE IV
Subdomains and Their Boundary Conditions

Ω_1 (PMs)	$r_{ri} \le r \le r_{ro}$ and $0 \le \varphi \le 2\pi$
At $r = r_{ri}$	$\partial\Phi_1/\partial r = 0$
At $r = r_{ro}$	$\Phi_1(r_{ro}, \varphi) = \Phi_2(r_{ro}, \varphi)$ and $\partial\Phi_1/\partial r = \partial\Phi_2/\partial r$
Ω_2 (air-gap):	$r_{ro} \le r \le r_{si}$ and $0 \le \varphi \le 2\pi$
Ω_{3i} (ith slot opening)	$r_{si} \le r \le r_{st}$ and $\phi_{s-} \le \varphi \le \phi_{s+}$ where $\phi_{s\pm} = \phi_{si} \pm \phi_{so}/2$
At $\varphi = \phi_{s\pm}$	$\partial\Phi_{3i}/\partial r = 0$
At $\varphi \in [\phi_{s-}, \phi_{s+}], r = r_{si}$	$\partial\Phi_2/\partial r = \partial\Phi_{3i}/\partial r$
At $\varphi \in [\phi_{s-}, \phi_{s+}], r = r_{si}$	$\partial\Phi_{3i}/\partial r = \partial\Phi_{4i}/\partial r$
Ω_{4i} (ith slot)	$r_{st} \le r \le r_{sb}$ and $\phi_{b-} \le \varphi \le \phi_{b+}$ where $\phi_{b\pm} = \phi_{si} \pm \phi_{sb}/2$
At $\varphi = \phi_{b\pm}$	$\partial\Phi_{4i}/\partial\varphi = 0$
At $\varphi \in [\phi_{s\pm}, \phi_{b\pm}], r = r_{st}$ and $\varphi \in [\phi_{b-}, \phi_{b+}], r = r_{sb}$	$\partial\Phi_{4i}/\partial r = 0$

Appendix A

Forward Torque Model

Fig. 7 shows the parameters for solving the MFD in the air-gap, where the stator slot/PM module in the 2-D plane is divided into four subdomains (see Table IV) to account for the effects of the slot tooth-tips on the solutions to the MFD. In Table IV, ϕ_{si}, ϕ_{so}, and ϕ_{sb} are the ith slot angular position, slot-opening angle and slot pitch; r_{ri}, r_{st}, and r_{sb} are the rotor-core radius, slot tooth-tip outer radius, and stator yoke radius. The slot and slot-opening in Fig. 7 are fan-shaped to accommodate the polar coordinates.

The scalar potential Φ in each subdomain is governed by the Poisson's equation. In polar coordinates

$$\nabla^2\Phi = \mu_o \begin{cases} \left(\partial M_r/\partial\varphi\right)/r - \partial M_t/\partial r & \Omega_1 \\ 0 & \Omega_2, \Omega_{3i} \\ -J_i \; (i = 1, 2 \ldots N_s) & \Omega_{4i} \end{cases} \tag{A.1a}$$

where $\nabla^2 = \frac{\partial^2}{\partial r^2} + \frac{\partial}{r\partial r} + \frac{\partial^2}{r^2\partial\varphi^2}$; J_i is the current density in the ith slot and the components of $\mathbf{M}$ along the radial and tangential directions are written in Fourier series expansion

$$M_r(\theta,\varphi) = \sum_{n=1,3,5\ldots}^{\infty} M_{rn} C_{nN_P(\varphi-\theta)} \tag{A.1b}$$

$$M_t(\theta,\varphi) = \sum_{n=1,3,5\ldots}^{\infty} M_{tn} S_{nN_P(\varphi-\theta)} \tag{A.1c}$$

In (A.1b) and (A.1c), $C_{(\cdot)} = \cos(\cdot)$ and $S_{(\cdot)} = \sin(\cdot)$for simplicity. Along with the boundary conditions in Table IV, the overall scalar potential Φ can be analytically solved using the separation of variable method from (A.1), which takes the form

$$\Phi(r,\varphi) = \sum_{k=1}^{K} \begin{bmatrix} \left(C_{sk+}\left(\frac{r}{r_{si}}\right)^{k} + C_{sk-}\left(\frac{r}{r_{ro}}\right)^{-k}\right) S_{k\varphi} \\ + \left(C_{ck+}\left(\frac{r}{r_{si}}\right)^{k} + C_{ck-}\left(\frac{r}{r_{ro}}\right)^{-k}\right) C_{k\varphi} \end{bmatrix} \tag{A.2a}$$

where K is the number of harmonics being considered. The coefficients $(C_{sk\pm}, C_{ck\pm})$ and hence Φ of the four subdomains are simultaneously solved. Once Φ is known, the MFDs (B_r, B_t) can be derived from (A.2b)

$$B_r(r,\varphi) = \frac{\partial\Phi(r,\varphi)}{r\partial\varphi} \text{ and } B_t(r,\varphi) = -\frac{\partial\Phi(r,\varphi)}{\partial r}. \tag{A.2b}$$

Setting the source item of Ω_1 and all Ω_{4i} zero in (A.1a), respectively, (B_{rE}, B_{tE}) and (B_{rP}, B_{tP}) can be obtained. Cogging torque $T_{\text{cog}}(\theta)$ and then the vectors a_m can be calculated from (B_{rP}, B_{tP}) and (B_{rE}, B_{tE}) by exciting only the mth phase coils with a constant current i_m, as defined in (A.3)

$$a_m(\theta) = [\tau - T_{\text{cog}}(\theta)]/i_m. \tag{A.3}$$

Appendix B

Lorentz Force in Harmonic Form

From (9a) and (9b)

$$\mathbf{a}(\theta)\mathbf{x} = \sum_{j=1,3\ldots}^{\infty}\sum_{k=1,3\ldots}^{\infty}\left[a_j i_{mk}\sum_{m=1}^{N_{ph}}\sin(j\theta_m)\sin(k\theta_m+\alpha_k)\right].$$

Using the product-to-sum formula in trigonometric identities

$$2S_{j\theta_m}S_{k\theta_m-\alpha_k} = C_{\theta_- - M_-} - C_{\theta_+ - M_+} \tag{B.1}$$

where $\theta_\pm = (j\pm k)(N_P\theta - \phi_1) \pm \alpha_k$ and $M_\pm = (2\pi/N_{ph})(j\pm k)(m-1)$.

In (B.1), $\theta_\pm$ do not depend on m. For an odd N_{ph}

$$\begin{aligned}\sum_{m=1}^{N_{ph}} C_{\theta_\pm - M_\pm} &= C_{\theta_\pm} + \sum_{m=2}^{(N_{ph}+1)/2}\left[C_{\theta_\pm - M_\pm} + C_{\theta_\pm-(2\pi - M_\pm)}\right] \\ &= C_{\theta_\pm}\left(\cos 0 + 2\sum_{m=2}^{(N_{ph}+1)/2} C_{M_\pm}\right) \\ &= C_{\theta_\pm}\xi_{j\pm k}\end{aligned}$$

where $\xi_{j\pm k} = \sum_{m=1}^{N_{ph}} C_{M_\pm}$.

For an even $N_{ph} = 2^K N_o$ with integer $K \geq 1$ and odd number N_o

$$\begin{aligned}\sum_{m=1}^{N_{ph}} C_{\theta_\pm - M_\pm} &= \sum_{m=1}^{N_{ph}/2}\left[C_{\theta_\pm - M_\pm} + C_{\theta_\pm - M_\pm - \pi(j\pm k)}\right] \\ &= \left[1+(-1)^{j\pm k}\right]\sum_{m=1}^{N_{ph}/2} C_{\theta_\pm - M_\pm} \\ &= \prod_{k=0}^{K-1}\left[1+(-1)^{\frac{j\pm k}{2^k}}\right] C_{\theta_\pm}\sum_{m=1}^{N_o} C_{M_\pm} = C_{\theta_\pm}\xi_{j\pm k}.\end{aligned}$$

Hence, (B.1) for a given phase number N_{ph} can be written as

$$\sum_{m=1}^{N_{ph}} S_{j\theta_m}S_{k\theta_m-\alpha_k} = \frac{N_{ph}}{2}\left(\xi_- C_{\theta_-} - \xi_+ C_{\theta_+}\right) \tag{B.2}$$

$$\xi_{j\pm k} = \begin{cases} C_{\frac{\pi}{2}+\frac{\pi(j\pm k)}{N_{ph}}}\sum_{m=1}^{N_{ph}} C_{M_\pm + \frac{\pi}{2}+\frac{\pi(j\pm k)}{N_{ph}}} = 0 & j\pm k \neq \ell N_{ph} \\ 1 & j\pm k = \ell N_{ph}\end{cases}. \tag{B.3}$$

Equation (13a) can be rewritten as

$$\begin{aligned}\mathbf{a}(\theta)\mathbf{x} = &\sum_{j=1,3\ldots}^{\infty}\sum_{k=1,3\ldots}^{\infty}\frac{N_{ph}a_j i_{mk}}{2} \\ &\times\left[\xi_{j-k}C_{(\theta_{j-k}-\alpha_k)} - \xi_{j+k}C_{(\theta_{j+k}+\alpha_k)}\right].\end{aligned}$$

References

[1] M. Villani, M. Tursini, G. Fabri, and L. Castellini, "High reliability permanent magnet brushless motor drive for aircraft application," *IEEE Trans. Ind. Electron.* vol. 59, no. 5, pp. 2073–2081, May 2012.

[2] J. A. Haylock, B. C. Mecrow, A. G. Jack, and D. J. Atkinson, "Operation of a fault tolerant PM drive for an aerospace fuel pump application, " *IEE Proc. Elect. Power Appl.*, vol. 145, no. 5, pp. 441–448, Sep. 1998.

[3] P. Zheng, Y. Sui, J. Zhao, C. Tong, T. A. Lipo, and A. Wang, "Investigation of a novel five-phase modular permanent-magnet in-wheel motor," *IEEE Trans. Magn.* vol. 47, no. 10, pp. 4084–4087, Oct. 2011.

[4] K. Bai, K.-M. Lee, J. Cao, R. Xu, and L. Li, "Design and decoupled compensation methods of a PM motor capable of 6D force/torque actuation for minimum bearing reaction," *IEEE/ASME Trans. Mechatronics*, vol. 22, no. 5, pp. 2252–2264, Oct. 2017.

[5] F. Barrero and M. J. Duran, "Recent advances in the design, modeling, and control of multiphase machines—Part I, " *IEEE Trans. Ind. Electron.* vol. 63, no. 1, pp. 449–458, Jan. 2016.

[6] M. R. Islam, "*Cogging Torque, Torque Ripple and Radial Force Analysis of Permanent Magnet Synchronous Machines*," *Ph.D. dissertation*, Dept. Elect. Eng., Univ. Akron, Akron, OH, USA, 2009.

[7] F. Scuiller, "Magnet shape optimization to reduce pulsating torque for a five-phase permanent-magnet low-speed machine," *IEEE Trans. Magn.* vol. 50, no. 4, pp. 1–9, Apr. 2014.

[8] K. Wang, Z. Q. Zhu, and G. Ombach, "Torque improvement of five-phase surface-mounted permanent magnet machine using third-order harmonic," *IEEE Trans. Energy Convers.*, vol. 29 no. 3, pp. 735–747, Sep. 2014.

[9] K. Wang, Z. Y. Gu, Z. Q. Zhu, and Z. Z. Wu, "Optimum injected harmonics into magnet shape in multiphase surface-mounted PM machine for maximum output torque," *IEEE Trans. Ind. Electron.*, vol. 64, no. 6, pp. 4434–4443, Jun. 2017.

[10] L. Zhu, S. Z. Jiang, Z. Q. Zhu, and C. C. Chan, "Analytical methods for minimizing cogging torque in permanent-magnet machines," *IEEE Trans. Magn.*, vol. 45, no. 4, pp. 2023–2031, 2009.

[11] I. Petrov, P. Ponomarev, Y. Alexandrova, and J. Pyrhönen, "Unequal teeth widths for torque ripple reduction in permanent magnet synchronous machines with fractional-slot non-overlapping windings," *IEEE Trans. Magn.* vol. 51, no. 2, pp. 1–9, Feb. 2015.

[12] A. Kais, J. Wang, and D. Howe, "Torque-ripple minimization in modular permanent-magnet brushless machines," *IEEE Trans. Ind. Appl.* vol. 39, no. 6, pp. 1689–1695, Nov./Dec. 2003.

[13] Y. Cho, K. B. Lee, J.-H. Song, and Y. I. Lee, "Torque-ripple minimization and fast dynamic scheme for torque predictive control of permanent-magnet synchronous motors," *IEEE Trans. Power Electron.*, vol. 30, no. 4, pp. 2182–2190, Apr. 2015.

[14] K. Jezernik, J. Korelič, and R. Horvat, "PMSM sliding mode FPGA-based control for torque ripple reduction," *IEEE Trans. Power Electron.*, vol. 28, no. 7, pp. 3549–3556, Jul. 2013.

[15] Z. Zhou, C. Xia, Y. Y, Z. Wang, and T. Shi, "Torque ripple minimization of predictive torque control for PMSM with extended control set," *IEEE Trans. Ind. Electron.*, vol. 64, no. 9, pp. 6930–6939, Sep. 2017.

[16] P. L. Chapman, S. D. Sudhoff, and C. A. Whitcomb, "Optimal current control strategies for surface-mounted permanent-magnet synchronous machine drives," *IEEE Trans. Energy Convers.*, vol. 14, no. 4, pp. 1043–1050, Dec. 1999.

[17] G. Feng, C. Lai and N. C. Kar, "An analytical solution to optimal stator current design for PMSM torque ripple minimization with minimal machine losses," *IEEE Trans. Ind. Electron.*, vol. 64, no. 10, pp. 7655–7665, Oct. 2017

[18] D. Flieller, N. K. Nguyen, P. Wira, G. Sturtzer, D. O. Abdeslam and J. Merkle, "A self-learning solution for torque ripple reduction for nonsinusoidal permanent-magnet motor drives based on artificial neural networks," *IEEE Trans. Ind. Electron.*, vol. 61, no. 2, pp. 655–666, Feb. 2014.

[19] M.-W. Naouar, E. Monmasson, A. A. Naassani, I. S. Belkhodja, and N. Patin, "FPGA-based current controllers for AC machine drives—A review," *IEEE Trans. Ind. Electron.* vol. 54, no. 4, pp. 1907–1925, Aug. 2007.

[20] J. Böcker, "Can oversampling improve the dynamics of PWM controls," in *Proc.IEEE Int. Conf. Ind. Technol.*, 2013, pp. 1818–1824.

[21] Z. Sun, J. Wang, G. W. Jewell, and D. Howe, "Enhanced optimal torque control of fault-tolerant PM machine under flux-weakening operation," *IEEE Trans. Ind. Electron.*, vol. 57, no. 1, pp. 344–353, Jan. 2010.

[22] A. Rahideh and T. Korakianitis, "Analytical magnetic field distribution of slotless brushless PM motors. Part 2: Open-circuit field and torque calculations," *IET Elect. Power Appl.*, vol. 6, no. 9, pp. 639–651, Nov. 2012.

[23] T. Lubin, S. Mezani, and A. Rezzoug, "2-D exact analytical model for surface-mounted permanent-magnet motors with semi-closed slots," *IEEE Trans. Magn.*, vol. 47, no. 2, pp. 479–492, Feb. 2011.

[24] L. J. Wu, Z. Q. Zhu, D. Staton, M. Popescu, and D. Hawkins, "Subdomain model for predicting armature reaction field of surface-mounted permanent-magnet machines accounting for tooth-tips," *IEEE Trans. Magn.*, vol. 47, no. 4, pp. 812–822, Apr. 2011.

[25] B. Hannon, P. Sergeant and L. Dupré, "Time-and spatial-harmonic content in synchronous electrical machines," *IEEE Trans. Magn.* vol. 53, no. 3, pp. 1–11, Mar. 2017.

[26] J. A. Haylock, "*Fault Tolerant Drives for Safety Critical Applications*," *Ph.D. dissertation*, Dept. Elect., Electron. Comput. Eng., Newcastle Univ., Newcastle upon Tyne, U.K., 1998.

[27] A. M EL-Refaie, Z. Q. Zhu, T. M. Jahns, and D. Howe, "Winding inductances of fractional slot surface-mounted permanent magnet brushless machines," *COMPEL – Int. J. Comput. Math. Elect. Electron. Eng.*, vol. 28, no. 6, pp. 1590–1606, 2009.

Lei Li received the B.S. degree in mechanical engineering from Tianjin University, Tianjin, China, in 2012. He is currently working toward the Ph.D. degree with Zhejiang University, Hangzhou, China.

He was a Visiting Scholar with the George W. Woodruff School of Mechanical Engineering, Georgia Institute of Technology, Atlanta, GA, USA, from 2016 to 2017. His research interests include system dynamics/control and mechatronics.

Kok-Meng Lee (M'89–SM'02–F'05) received the B.S. degree in mechanical engineering from the State University of New York, Buffalo, NY, USA, in 1980, and the S.M. and Ph.D. degrees in mechanical engineering from the Massachusetts Institute of Technology, Cambridge, MA, USA, in 1982 and 1985, respectively.

He is currently a Professor with the George W. Woodruff School of Mechanical Engineering, Georgia Institute of Technology, Atlanta, GA, USA. He is also a Distinguished Professor with the State Key Laboratory of Digital Manufacturing Equipment and Technology, Huazhong University of Science and Technology, Wuhan, China, under the National Recruitment Program of Global Experts. He was a Pao Yu-Kong Chair Professor with Zhejiang University, Hangzhou, China. He holds eight patents in machine vision, three-degree-of-freedom spherical motor/encoder, and live-bird handling system. His research interests include system dynamics/control, robotics, automation, and mechatronics.

Dr. Lee is a Fellow of the American Society of Mechanical Engineers. He was the recipient of the National Science Foundation Presidential Young Investigator, Sigma Xi Junior Faculty Research, International Hall of Fame New Technology, and Kayamori Best Paper Awards.

Kun Bai (M'13) received the B.S. degree in control science and engineering from Zhejiang University, Hangzhou, China, in 2006, and the M.S. and Ph.D. degrees in mechanical engineering from Georgia Institute of Technology, Atlanta, GA, USA, in 2009 and 2012, respectively.

He is currently an Associate Professor with the State Key Laboratory of Digital Manufacturing Equipment and Technology and the School of Mechanical Science and Engineering, Huazhong University of Science and Technology, Wuhan, China. His research interests include smart electromagnetic actuators/sensors and novel applications.

Xiaoping Ouyang received the B.S. and M.S. degrees from Northeast Petroleum University, Anda, China, in 1997 and 2000, respectively, and the Ph.D. degree from Zhejiang University, Hangzhou, China, in 2005, all in mechanical engineering.

He is currently a Professor with the State Key Laboratory of Fluid Power and Mechatronic Systems, Department of Mechanical Engineering, Zhejiang University, Hangzhou, China. His current research interests include electrohydraulic system control, aircraft hydraulics, and exoskeleton robots.

Huayong Yang received the B.S. degree in mechanical engineering from Huazhong University of Science and Technology, Wuhan, China, in 1982, and the Ph.D. degree in mechanical engineering from the University of Bath, Bath, U.K., in 1988.

Since 1989, he has been with Zhejiang University, Hangzhou, China, where he is the Director of the State Key Laboratory of Fluid Power and Mechatronic Systems and the School of Mechanical Engineering. His current research interests include motion control and energy saving of mechatronic systems, fluid power components, and system development.

Dr. Yang is an Academician of the Chinese Academy of Engineering. He was the recipient of the first class of the National Scientific and Technological Progress Award, the National Outstanding Researcher of the Natural Science Foundation of China, and three Ministerial or Provincial Scientific and Technological Progress Prizes.